JEM

The Journal of Experimental Medicine

Myocyte necrosis underlies progressive myocardial dystrophy in mouse *dsg2*-related arrhythmogenic right ventricular cardiomyopathy

Kalliopi Pilichou,[1,3] Carol Ann Remme,[3] Cristina Basso,[1]
Maria E. Campian,[3] Stefania Rizzo,[1] Phil Barnett,[3] Brendon P. Scicluna,[3]
Barbara Bauce,[2] Maurice J.B. van den Hoff,[3] Jacques M.T. de Bakker,[3]
Hanno L. Tan,[3] Marialuisa Valente,[1] Andrea Nava,[2] Arthur A.M. Wilde,[3]
Antoon F.M. Moorman,[3] Gaetano Thiene,[1] and Connie R. Bezzina[3]

[1]Department of Medical Diagnostic Sciences and Special Therapies and [2]Department of Cardiac, Thoracic, and Vascular Sciences, University of Padua, 35121 Padua, Italy
[3]Heart Failure Research Center, Academic Medical Center, University of Amsterdam, 1105 AZ Amsterdam, Netherlands

Mutations in the cardiac desmosomal protein desmoglein-2 (*DSG2*) are associated with arrhythmogenic right ventricular cardiomyopathy (ARVC). We studied the explanted heart of a proband carrying the *DSG2*-N266S mutation as well as transgenic mice (Tg-NS) with cardiac overexpression of the mouse equivalent of this mutation, N271S-*dsg2*, with the aim of investigating the pathophysiological mechanisms involved. Transgenic mice recapitulated the clinical features of ARVC, including sudden death at young age, spontaneous ventricular arrhythmias, cardiac dysfunction, and biventricular dilatation and aneurysms. Investigation of transgenic lines with different levels of transgene expression attested to a dose-dependent dominant-negative effect of the mutation. We demonstrate for the first time that myocyte necrosis is the key initiator of myocardial injury, triggering progressive myocardial damage, including an inflammatory response and massive calcification within the myocardium, followed by injury repair with fibrous tissue replacement, and myocardial atrophy. These observations were supported by findings in the explanted heart from the patient. Insight into mechanisms initiating myocardial damage in ARVC is a prerequisite to the future development of new therapies aimed at delaying onset or progression of the disease.

CORRESPONDENCE
Connie R. Bezzina:
C.R.Bezzina@amc.uva.nl

Abbreviations used: ANOVA, analysis of variance; ARVC, arrhythmogenic right ventricular cardiomyopathy; *DSG2*, desmoglein-2; EBD, Evans blue dye; ECG, electrocardiography; HW/BW, heart weight to body weight; LV, left ventricle; LVEF and RVEF, LV and RV ejection fraction, respectively; RV, right ventricle; TUNEL, terminal deoxynucleotidyl transferase–mediated dUTP nick-end labeling; VT, ventricular tachycardia.

Arrhythmogenic right ventricular cardiomyopathy (ARVC; Online Mendelian Inheritance in Man accession no. 107970) is a clinically and genetically heterogeneous cardiac inherited disorder estimated to affect ∼1:2,000–5,000 individuals and is associated with increased risk of sudden death (Marcus et al., 1982; Thiene et al., 1988; Marcus et al., 2007; Basso et al., 2009). The pathological hallmark of ARVC consists of progressive, diffuse or segmental loss of cardiac myocytes. These are replaced by fibrofatty tissue predominantly in the right ventricle (RV), with aneurysm formation, chamber dilatation, and impaired cardiac function (Thiene et al., 1988; Basso et al., 1996). Clinical characteristics of the disease comprise left bundle branch block morphology ventricular arrhythmias, frequently associated with syncope or sudden cardiac death. Disease onset typically occurs in teenage years or young adulthood. It particularly affects athletes, in whom it is believed to be responsible for up to 20% of sudden cardiac death cases (Corrado et al., 2006).

Nearly half of ARVC probands harbor one or more mutations in genes encoding major components of cardiac desmosomes, including plakoglobin, desmoplakin, plakophilin-2, desmoglein-2 (*DSG2*), and desmocollin-2 (Rampazzo et al., 2002; Gerull et al., 2004;

The Rockefeller University Press $30.00
J. Exp. Med. Vol. 206 No. 8 1787-1802
www.jem.org/cgi/doi/10.1084/jem.20090641

Pilichou et al., 2006; Syrris et al., 2006; Asimaki et al., 2007). Inheritance is mainly autosomal dominant with variable penetrance and expressivity. Homozygous mutation in the plakoglobin gene causes Naxos disease, whereas homozygous mutation in the desmoplakin gene underlies Carvajal syndrome, both characterized by ARVC associated with hair and skin abnormalities (McKoy et al., 2000; Norgett et al., 2000).

Despite recent discoveries on the genetic basis of ARVC, the etiopathogenesis of the disease remains poorly understood. Different mechanisms have been proposed to underlie the ARVC phenotype. In earlier years, the disontogenetic (dysplastic), the degenerative (dystrophic), and the inflammatory theories have been suggested (Thiene et al., 1991; Basso et al., 1996). In addition, cardiomyocyte apoptosis has been associated with ARVC, but the contribution of programmed cell death in disease onset (Mallat et al., 1996; Valente et al., 1998) and progression remains unclear. In 2006, three animal models were generated in an attempt to define pathogenetic mechanisms of ARVC. These genetically engineered mice supported the transdifferentiation theory, the impairment of desmosomal function theory, and the role of environmental contribution to disease expression, respectively (Garcia-Gras et al., 2006; Kirchhof et al., 2006; Yang et al., 2006). However, the sequence of cellular events characterizing disease onset and progression remains unexplored.

We have previously identified the *DSG2*-N266S mutation in a small kindred with ARVC (Pilichou et al., 2006). The N266 residue, located between the second and third extracellular cadherin domains of *DSG2*, has been shown to be critical for coordination of Ca^{2+} binding, a phenomenon essential to the adhesive intercellular interactions of junctional cadherins. In the present study, we have analyzed a mouse model with overexpression of the mouse homologue of this mutation, N271S-*dsg2*, and investigated the explanted heart of the proband with the N266S mutation, enabling comparison of clinicopathological findings with the animal model. We demonstrate for the first time that myocyte necrosis is a key initiator of myocardial injury in ARVC, triggering progressive myocardial damage.

RESULTS

Clinical features in the proband carrying the *DSG2*-N266S mutation

The proband, a 55-yr-old female at diagnosis, was hospitalized for an episode of sustained ventricular tachycardia (VT) with left bundle branch block morphology that was hemodynamically well tolerated. 12-lead electrocardiography (ECG) showed sinus rhythm with first-degree atrioventricular block and negative T waves in V1–V3. Signal-averaged ECG demonstrated late potentials at all filter settings (25, 40, and 80 Hz). Two-dimensional echocardiography and ventricular angiography displayed severe RV dilatation with a mildly depressed function (RV ejection fraction [RVEF]: 48%), whereas left ventricle (LV) parameters were within normal limits. Normal, patent coronary arteries were observed at coronary angiography. The patient received an implantable cardioverter-defibrillator a year later. During follow-up, she had progression of the disease with T wave inversion up to V5 and low QRS voltages on 12-lead ECG, and decreasing RV function (RVEF: 35%) in addition to signs of LV involvement on echocardiography (LVEF: 47%; Fig. 1, A and B). Moreover, the patient experienced several episodes of sustained VT and developed signs and symptoms of heart failure at the age of 63. Renal function remained normal until the last follow-up. Because of refractory heart failure, she eventually underwent successful heart transplantation at the age of 65. Clinical and genetic data on family members have been reported previously (Pilichou et al., 2006).

Pathological findings in the explanted heart of the proband

The explanted heart of the proband revealed increased heart weight (450 g), biventricular chamber dilatation (Fig. 1 C), wall thinning (RV free-wall thickness, 1 mm; LV free-wall thickness, 7 mm; ventricular septum thickness, 10 mm), and RV aneurysms at the inflow, apex, and outflow regions with endocardial thrombosis, in the presence of normal epicardial coronary arteries. Histologically, diffuse myocardial atrophy with fibro-fatty replacement was evident, which extended transmurally throughout the RV free wall and was confined to the subepicardial and midmural layers of the LV free wall (Fig. 1, D–F). The residual myocytes showed hypertrophy with dysmorphic and dysmetric nuclei. Spots of calcification (Fig. 1 G) were evident both in the RV and LV myocardium, typically within areas of dense fibrous tissue. Scanty inflammatory infiltrates, consisting mostly of T lymphocytes, were also observed.

Generation of transgenic mice with cardiac-restricted expression of N271S-*dsg2*

We generated transgenic mice with cardiac-specific overexpression of FLAG-tagged WT *dsg2* (Tg-WT) and N271S-*dsg2* (Tg-NS). Two founders were obtained for Tg-WT and three founders for Tg-NS. Offspring from one of the Tg-WT founders and two of the Tg-NS founders were used in this study. The two Tg-NS lines studied differed in their level of expression of N271S mutant FLAG-tagged *dsg2* and were designated Tg-NS/H (high expression) and Tg-NS/L (low expression; Fig. S1 A). The cardiac expression level of FLAG-tagged WT *dsg2* in the Tg-WT line studied was similar to Tg-NS/H. Confocal microscopy on cryosections of cardiac tissue stained with anti-FLAG antibody demonstrated proper localization of FLAG-tagged *dsg2* to the intercalated discs in all three mouse lines studied (Fig. S1 B).

Sudden death occurred in 30% of mice with high expression of N271S-*dsg2* (Tg-NS/H) by the age of 3.6 wk, and only 20% of Tg-NS/H mice survived by the age of 20 wk (Fig. 2 A). In contrast, mice expressing lower levels of N271S-*dsg2* (Tg-NS/L) died at an older age (30% incidence of sudden death by the age of 6.2 wk).

ECG

Representative examples of surface ECG recordings from WT, Tg-WT, and Tg-NS/H mice are depicted in Fig. 2 (B and C), and the main electrocardiographic data are reported in Fig. 2 D and Table S1. At an average age of ∼6 wk, Tg-NS/H mice displayed significantly increased QRS duration compared with WT and Tg-WT mice, whereas no differences in either heart rate (RR interval), PR duration, or QTc interval were observed. Tg-NS mice also displayed significantly more spontaneous arrhythmias compared with WT and Tg-WT mice. Tg-NS mice displayed frequent premature

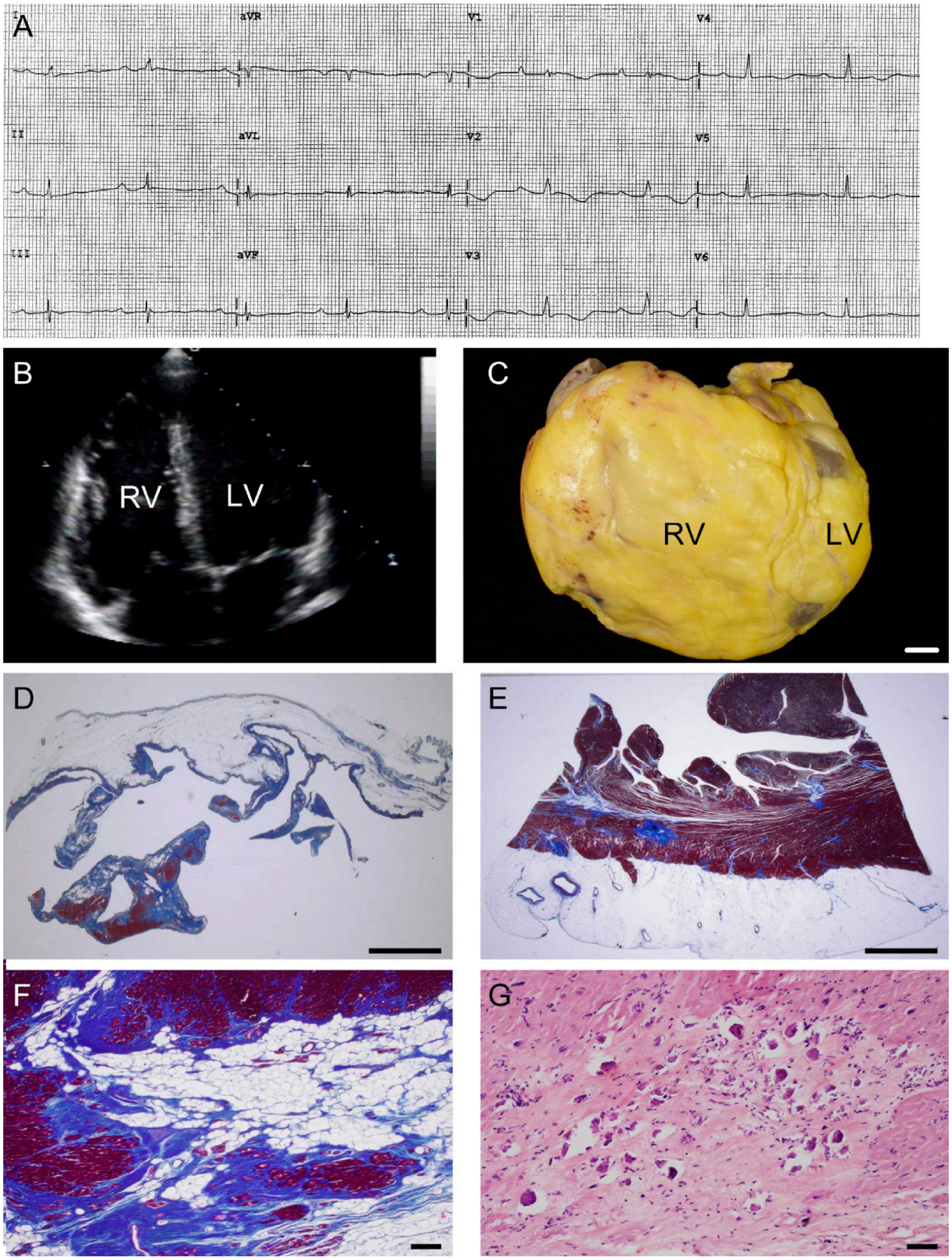

Figure 1. Characteristics of the female patient carrier of the *DSG2*-N266S mutation who underwent heart transplantation at the age of 65. (A) 12-lead ECG 2 mo before heart transplantation displaying sinus rhythm with PQ and QT prolongation, intraventricular conduction delay, and negative T wave V1–V4. (B) Two-dimensional echocardiography showing biventricular dilatation. (C) Gross view of the explanted heart specimen showing massive RV dilatation with RV outflow tract aneurysm. Bar, 1 cm. (D and E) RV and LV free wall showing fibro-fatty replacement of the myocardium with almost total disappearance of the myocardium in the RV. Bar, 5 mm. (F) Close-up of E. Bar, 30 µm. (G) At higher magnification, spotty calcification is observed in areas of replacement-type fibrosis. Bar, 50 µm.

ventricular beats, monomorphic and polymorphic VT, and atrial arrhythmias (Fig. 2 C), whereas WT and Tg-WT mice showed only sporadic atrial premature beats. In contrast to Tg-NS/H mice, those from the Tg-NS/L line showed no differences in ECG parameters at the age 6 wk but developed significant QRS prolongation only with advanced age, thus displaying a phenotype of intermediate severity (Table S2). Interestingly, Tg-NS/L mice displayed spontaneous arrhythmias already at young age in the presence of normal ECG indices (Table S1).

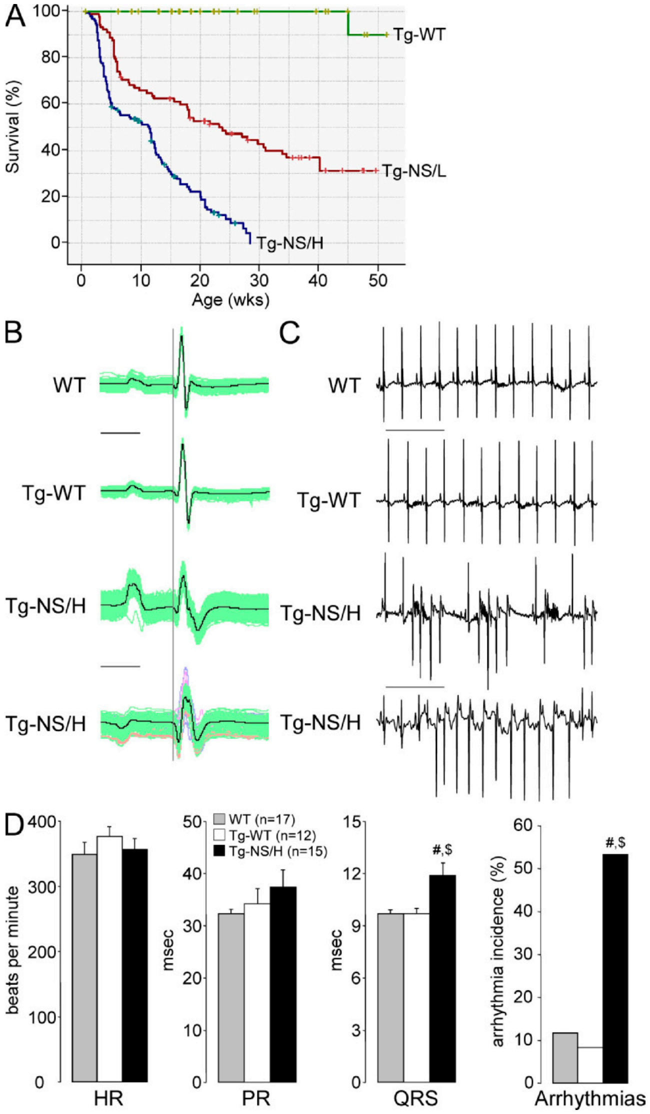

Figure 2. Characteristics of transgenic mice with cardiac-restricted expression of N271S-*dsg2*. (A) Kaplan-Meier survival plot of Tg-NS/H (blue line; *n* = 225), Tg-NS/L (red line; *n* = 156), and Tg-WT (green line; *n* = 129) mice. Note the high death rate in the mutant lines, with 30% of death occurring by 3.6 wk in Tg-NS/H mice. (B) Examples of surface ECG measurements from WT, Tg-WT, and Tg-NS/H mice showing prolongation and fractionation of the QRS complex, indicating impairment of ventricular conduction. Bar, 25 ms. (C) Typical ECG examples of spontaneous ventricular arrhythmias observed in Tg-NS/H mice. Bar, 500 ms. (D) Mean values of ECG parameters including heart rate (HR), PR and QRS intervals, and incidence of spontaneous arrhythmias. Data represent means ± SEM measured from >200 consecutive beats from single independent ECG measurements in 17 WT, 12 Tg-WT, and 15 Tg-NS/H mice (#, $P < 0.05$ vs. WT; $, $P < 0.05$ vs. Tg-WT; Table S1).

Cardiac morphology and function in vivo

Representative M-mode and two-dimensional echocardiograms performed in 12-wk-old mice are shown in Fig. 3 A. The main echocardiographic data are reported in Fig. 3 B and Table S3. Tg-NS/H mice showed increased RV and LV end-diastolic and -systolic diameters and increased RV end-diastolic area. LV fractional shortening was significantly reduced in Tg-NS/H compared with Tg-WT and WT mice. Tg-NS/L mice demonstrated a phenotype of intermediate severity (Table S3).

Conduction slowing and arrhythmia inducibility in isolated hearts

Data from epicardial mapping experiments performed on isolated Langendorff-perfused hearts are reported in Fig. 4 and Table S4. In hearts from Tg-NS/H mice, both RV and LV showed abnormal activation patterns in addition to crowding of isochrones, indicating the presence of conduction block (Fig. 4 A). During sinus rhythm, total ventricular activation time was significantly increased in both RV and LV of Tg-NS/H as compared with WT and Tg-WT mice (Fig. 4 E). When the hearts were stimulated from the center of the electrode at a basic cycle length of 120 ms, total activation time was greatly increased in LV of Tg-NS/H mice, whereas there was only a trend toward increased activation time observed for the RV (Fig. 4 E). Excessive conduction slowing in Tg-NS/H hearts was further associated with fractionation of the extracellular electrogram, a feature not observed in WT or Tg-WT hearts (Fig. 4 B). Tg-NS/H hearts also displayed increased inducibility of ventricular arrhythmias as compared with WT and Tg-WT hearts, both in LV and RV (Fig. 4, C, D, and F). A phenotype of intermediate severity was again observed on epicardial mapping in Tg-NS/L compared with Tg-NS/H hearts (Table S4).

Gross cardiac morphology

Main cardiac features and gross morphology data from the different study groups are displayed in Fig. 5. Gross morphological examination of the hearts from Tg-NS/H mice did not reveal any pathological change in mice younger than 2 wk (Fig. 5 A, a). In 3–5-wk-old Tg-NS/H mice, hearts were increased in weight and displayed whitish streaks in the subepicardial myocardium (Fig. 5 A, b). Progressive thinning of both the LV and the RV free walls was found with increasing age in Tg-NS/H mice. Moreover, Tg-NS/H mice >5 wk old showed RV and LV chamber dilatation and biventricular aneurysms (Fig. 5 A, c). With increasing age, Tg-NS/H hearts displayed significant increments of heart weight to body weight (HW/BW) ratio and cardiomyocyte diameter, and significant reduction of RV, LV, and ventricular septum wall thickness (Fig. 5 B). In line with previous observations (see above), Tg-NS/L hearts again showed an intermediate severity phenotype (Table S5).

Histological abnormalities

Trichrome, hematoxylin-eosin (H&E), and von Kossa staining on heart sections revealed no abnormalities in Tg-NS/H mice <2 wk old (Fig. 6, A–C; and Fig. 7 A). Spotty contraction band and coagulative necrosis, followed by massive inflammatory infiltrates, were evident in the myocardium of 2–3-wk-old Tg-NS/H mice (Fig. 6, D–F; Fig. 7 B; and Fig. 8, A and B) but not in Tg-WT and WT mice of the same age. In 3–5-wk-old Tg-NS/H mice, extensive myocyte necrosis and massive calcification were a constant feature in both RV and LV; granulation tissue and early loose connective tissue deposition were also evident (Fig. 6, G–I; and Fig. 7 C). Typically, myocardial damage started in the outer subepicardial layers (Fig. 6, D–F), with progressive extension toward the endocardium to become transmural by 4 wk (Fig. 6, G–I).

As revealed by trichrome staining, dense fibrosis with collagen bundle formation and aneurysm appeared in all

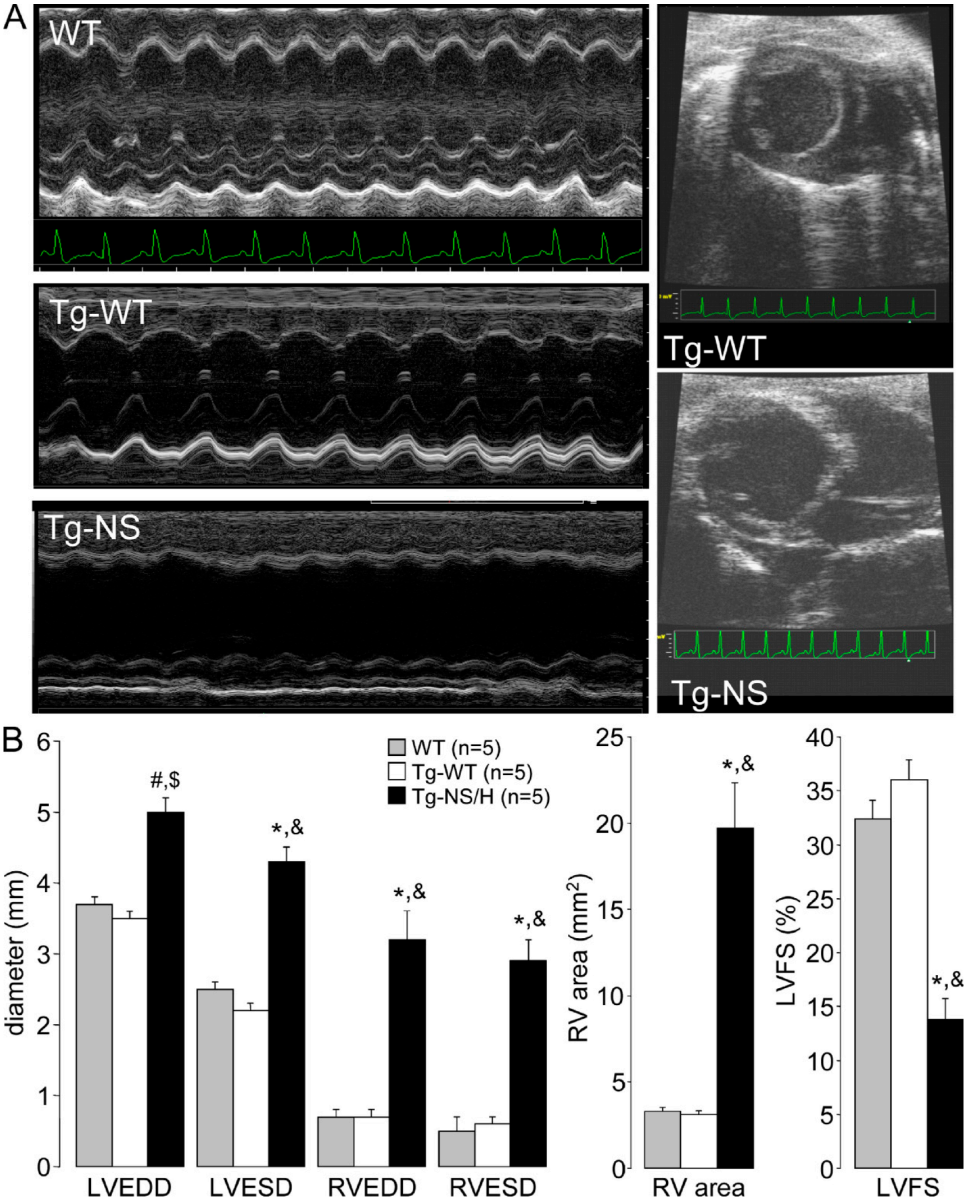

Figure 3. Assessment of in vivo cardiac morphology and function. (A) M-mode and two-dimensional echocardiography in WT, Tg-WT, and Tg-NS/H mice displaying LV and RV chamber dilatation in mutant mice. (B) Mean values of echocardiographic parameters from WT, Tg-WT, and Tg-NS/H mice, including LV and RV end-diastolic diameter (LVEDD and RVEDD, respectively), LV and RV end-systolic diameter (LVESD and RVESD, respectively), RV area (RV area in diastole [short-axis view]), and LV fractional shortening (LVFS). Data represent means ± SEM from single independent echocardiographic measurements on five mice per experimental group (#, $P < 0.05$ vs. WT; *, $P < 0.001$ vs. WT; $, $P < 0.01$ vs. Tg-WT; &, $P < 0.001$ vs. Tg-WT; Table S3).

Tg-NS/H mice >5 wk old (Fig. 6, J and M; and Fig. 7 D) but not in aged-matched Tg-WT and WT controls. Nuclear abnormalities (dysmetric and dysmorphic) were also evident in later stages.

Oil red O staining of thin myocardial sections showed focal lipid droplet accumulation, typically within the areas of myocyte necrosis (not depicted). No adipocytes were observed, both at early and late stages of disease.

Consistent with death at older age and the later development of echocardiographic and electrophysiological abnormalities, Tg-NS/L hearts showed a morphological phenotype of intermediate severity compared with Tg-NS/H

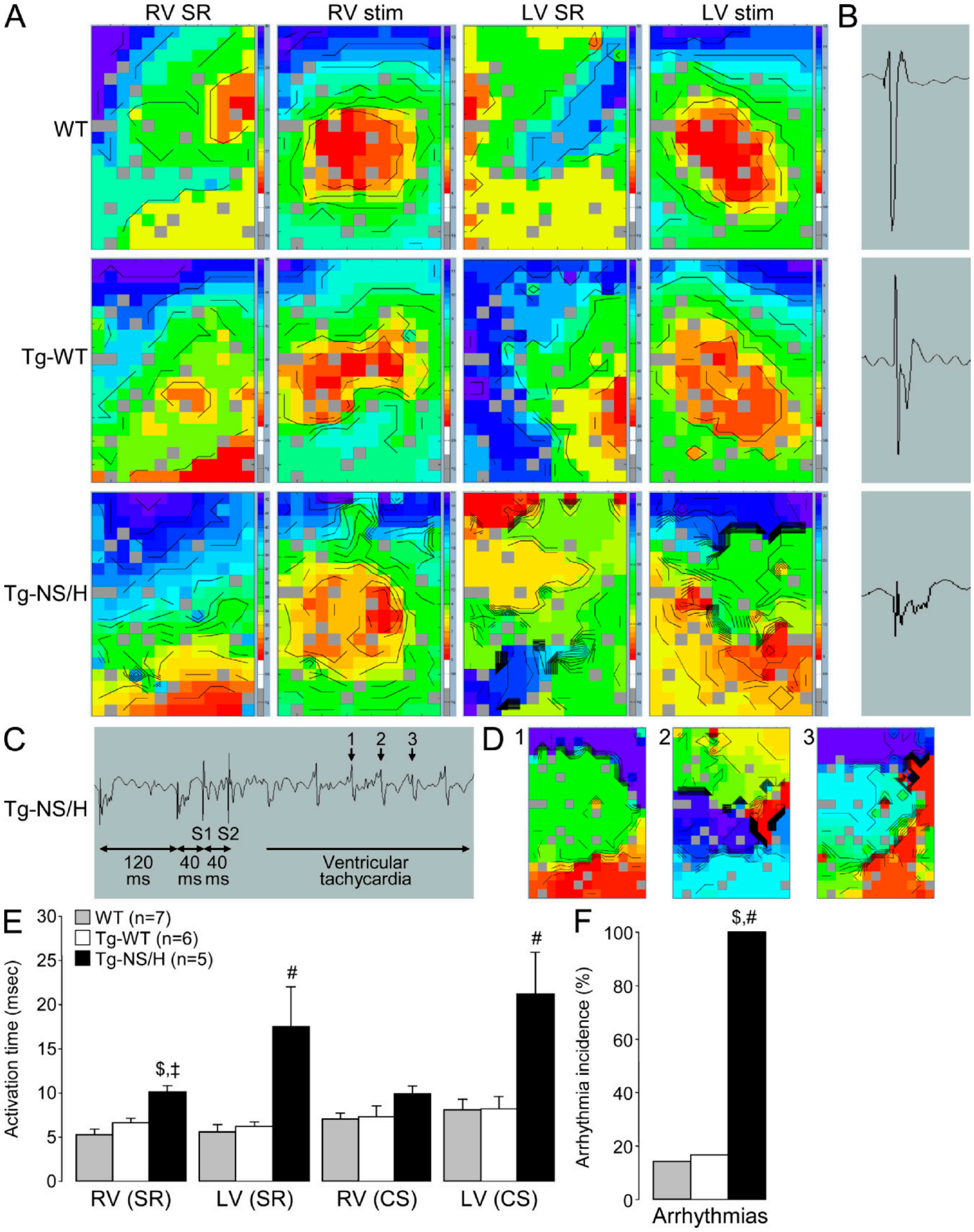

Figure 4. Epicardial mapping experiments in Langendorff-perfused hearts. (A) Examples of RV and LV activation maps for WT, Tg-WT, and Tg-NS/H hearts during sinus rhythm (SR) and stimulation from the center of the electrode (stim). Crowding of isochrones in Tg-NS/H hearts indicates areas of conduction slowing. (B) Examples of extracellular electrograms showing fractionation of the extracellular signal (a sign of excessive conduction slowing) in Tg-NS/H but not in WT or Tg-WT mice. (C) Induction of VT in a Tg-NS/H heart after administration of two short-coupled extrastimuli (S1 and S2). (D) Ventricular activation map during beats 1–3 of the VT depicted in C. (E) Mean RV and LV activation times during SR and central stimulation (CS). (F) Mean incidence of inducible arrhythmias. Data represent means ± SEM from single independent epicardial mapping experiments from five WT, six Tg-WT, and five Tg-NS/H mice (#, $P < 0.05$ vs. WT; ‡, $P < 0.01$ vs. WT; $, $P < 0.05$ vs. Tg-WT; Table S4).

hearts. These mice developed significant histological abnormalities only at older age (>5 wk) and showed lower prevalence of calcification, indicating a slower development of the phenotype.

Assessment of necrosis

Necrosis was the first manifestation of disease in all Tg-NS hearts studied. Electron microscopic evaluation in 2–3-wk-old Tg-NS/H mice showed ultrastructural features in

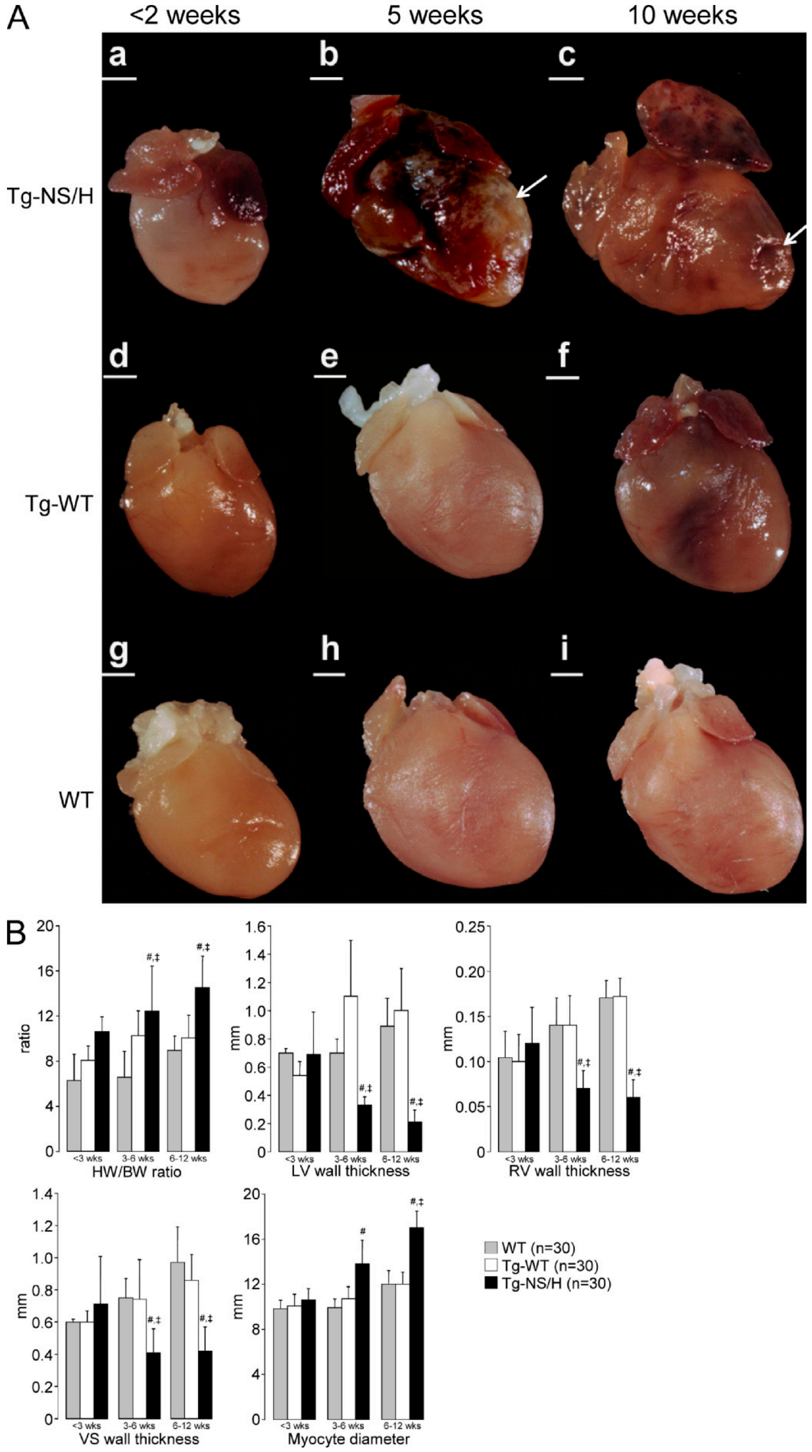

Figure 5. Gross features of explanted mouse hearts. (A) Tg-NS/H, Tg-WT, and WT hearts at age <2 (a, d, and g), 5 (b, e, and h), 10 (c, f, and i) wk. Note the structurally normal hearts at young age, with later appearance of calcification and dilatation with aneurysms (arrows) in Tg-NS/H hearts. Bars: (a, b, and d–i) 1 mm; (c) 2 mm. (B) Mean values of HW/BW ratios; LV, RV, and ventricular septum (VS) wall thicknesses; and cardiomyocyte diameters in hearts of different age groups (<3, 3–6, and 6–12 wk; 10 mice per age group for each line; #, $P < 0.01$ vs. WT; ‡, $P < 0.01$ vs. Tg-WT; Table S5).

keeping with cardiomyocyte necrosis, i.e., disruption of the sarcolemma, disgregation of myofilaments and other cytoplasmic elements, and mitochondrial swelling. Multiple amorphous matrix densities were observed in swollen mitochondria (Fig. 8, C and D). Some mitochondria also exhibited electron-dense calcific deposits and complete mineralization preceding calcification of cardiomyocytes (Fig. 8 E). Calcified cardiomyocytes were then phagocytosed by macrophages with typical lysosomal bodies. In older mice with advanced myocardial lesions, the remnants of necrotic myocytes were seen as scattered dense masses of mineralized debris with surrounding collagen bundles and occasional macrophages (Fig. 8 F).

To determine whether disruption of the sarcolemmal membrane occurred in the intact hearts of young (2–3 wk old) Tg-NS/H mice, we evaluated sarcolemmal integrity in vivo by injecting Evans Blue dye (EBD), a large tracer molecule that can only enter myocytes with a disrupted sarcolemma. Uptake of EBD was observed in the myocardium of Tg-NS/H mice but was absent in Tg-WT and WT mice (Fig. 9).

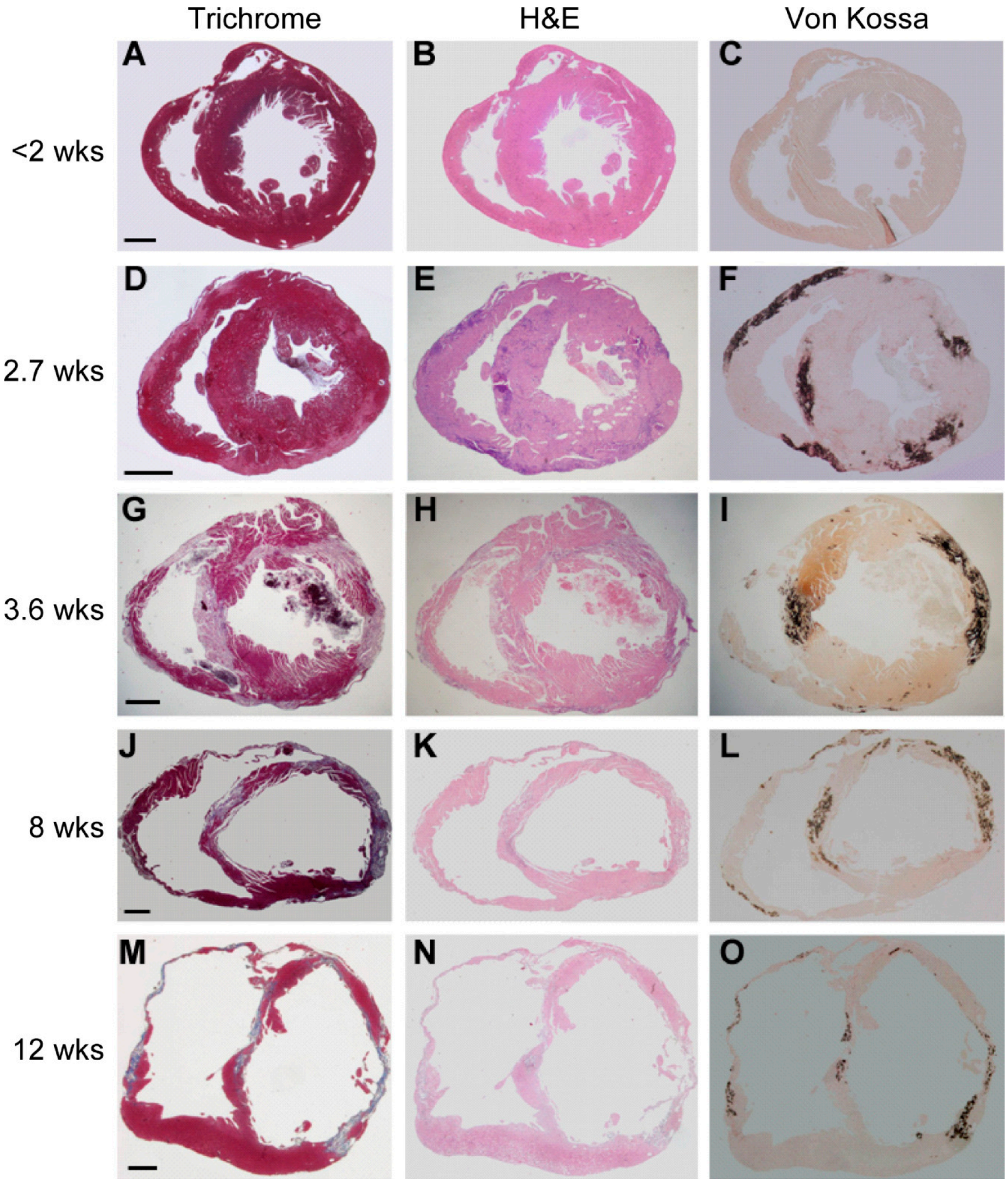

Figure 6. Histological features of explanted hearts from Tg-NS/H mice. (A–O) Heidenhain trichrome, H&E, and von Kossa staining of transverse full sections of the hearts at different ages: <2 (A–C), 2.7 (D–F), 3.6 (G–I), 8 (J–L), and 12 (M–O) wk. Note the appearance of myocardial damage in the outer subepicardial layers with calcification in both RV and LV free walls after 2 wk of age, with progressive extension to become transmural by 4 wk of age, and deposition of mature fibrosis with wall thinning and aneurysm formation by 8 wk of age. Bars: (A–C) 0.5 mm; (D–F) 0.8 mm; (G–I) 0.5 mm; (J–L) 0.4 mm; and (M–O) 0.8 mm.

Assessment of apoptosis

Terminal deoxynucleotidyl transferase–mediated dUTP nick-end labeling (TUNEL) analysis in 2–3-wk-old mice demonstrated low levels of positive cells in Tg-NS/H mice (Fig. 10 A). These were usually confined close to areas of myocyte necrosis and/or fibrous tissue replacement. A higher TUNEL index was found in Tg-NS/H mice compared with WT and Tg-WT mice at >6 wk of age.

Immunostaining with anticleaved caspase-3 antibody at >2 wk of age showed the presence of apoptotic cells in Tg-NS/H hearts, but again only in necrotic areas (Fig. 10 B). In contrast, at <2 wk of age, only sporadic cleaved caspase-3 positivity was observed, indicating that apoptosis did not precede the development of necrosis. Western blot analysis on cardiac tissue from 3- and 6-wk-old mice did not reveal an increment of cleaved caspase-3 levels in Tg-NS/H compared with Tg-WT and WT mice (unpublished data).

Assessment of intercalated discs

Electron microscopic evaluation of younger (<2 wk old) and older Tg-NS/H mice showed structurally normal desmosomes distributed along the intercalated discs, even in the setting of myocyte necrosis, that were similar to those of age-matched Tg-WT and WT hearts. In particular, no widened gaps of intercalated discs were observed in Tg-NS/H mice (Fig. S2). Immunohistochemical assessment by confocal microscopy of Tg-NS/H myocardium showed a normal distribution at the level of the intercalated discs of desmosomal proteins (desmoplakin, desmoglein-2, plakoglobin, and plakophilin-2), as well as desmin and connexin43 (unpublished data).

DISCUSSION

Transgenic mice overexpressing *dsg2*-N271S, the mouse homologue of the *DSG2*-N266S mutation found in a family with ARVC, recapitulate the pathognomonic features of the human disease, including sudden death, spontaneous ventricular arrhythmias, ECG characteristics of conduction slowing, cardiac dysfunction, ventricular dilatation and aneurysms, myocardial atrophy, and fibrosis. In this model, which is the first *dsg2*-related mouse model of ARVC, we provide evidence that the ARVC phenotype, although genetically determined, develops postnatally and is progressive with age. We demonstrate for the first time that it is initiated by necrotic cell death, which subsequently triggers an inflammatory response and massive calcification within the myocardium, followed later by injury repair with fibrous tissue replacement. Our data bring to the fore hitherto underexposed aspects in the pathogenesis of ARVC. Insight into the mechanism of disease enables research into new therapies aimed at delaying onset and progression of ARVC.

Cardiac desmosomes and *DSG2*

Cardiac desmosomes are intercellular junctions at the intercalated discs of cardiomyocytes, closely apposed to gap

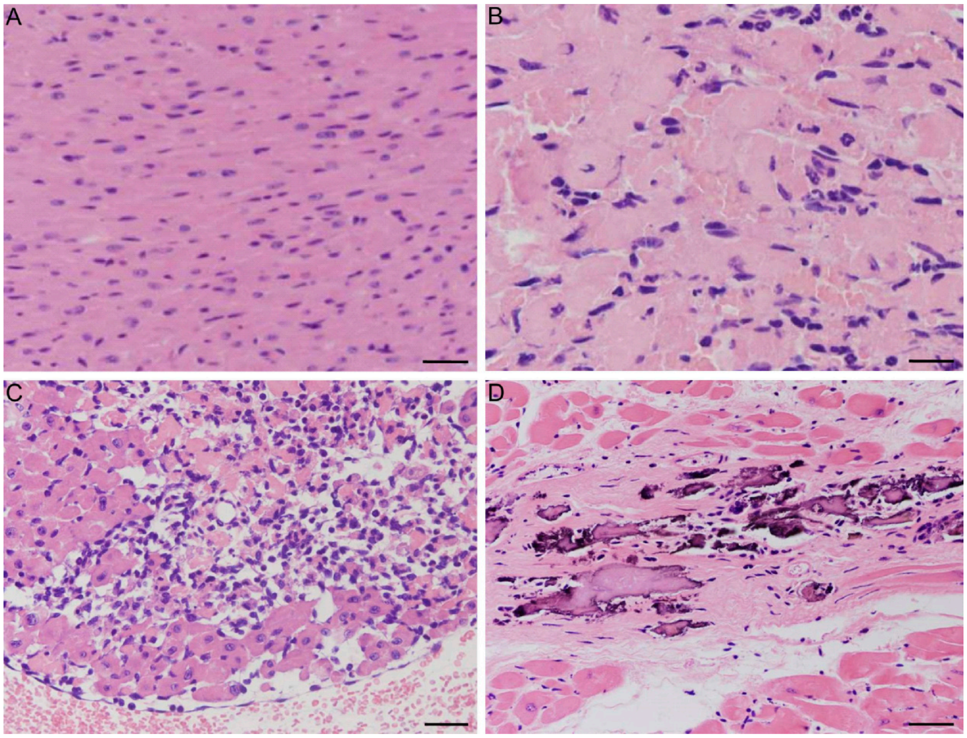

Figure 7. Histological features of Tg-NS/H hearts at high magnification. (A) Normal myocardium (1.7 wk of age). Bar, 50 µm. (B) Cardiomyocyte necrosis with early neutrophil infiltrates (2.1 wk of age). Bar, 20 µm. (C) Diffuse inflammatory cells including macrophages (3.6 wk of age). Bar, 50 µm. (D) Replacement-type fibrosis with spots of calcification (8 wk of age). Bar, 30 µm.

junction plaques, which confer mechanical coupling of the myocytes in the heart through families of proteins including the desmosomal cadherins, armadillo, and plakins (Stokes, 2007). The desmosomal cadherins (desmogleins and democollins) are single transmembrane glycoproteins, which mediate Ca^{2+}-dependent homophilic interactions between the extracellular regions of these proteins emanating from opposing cell surfaces. The intracellular domain of desmosomal cadherins binds to two proteins of the armadillo family, namely plakoglobin and plakophilin, forming an indirect link to desmoplakin and the intermediate filaments (desmin; Troyanovsky et al., 1993; Chitaev and Troyanovsky, 1997). Adhesion of cadherins originating from adjacent cells occurs through interaction of extracellular cadherin domains (ectodomains) that form the rodlike extracellular portion of the protein. Successive ectodomains are interconnected by sequences that dock three Ca^{2+} ions (Nagar et al., 1996). Structural and biochemical interaction studies of cadherin ectodomains have demonstrated the importance of Ca^{2+} binding at these sites in adhesive intercellular interactions of these domains, providing structural rigidity necessary for recognition and assembly of trans (adhesive) cadherin junctions

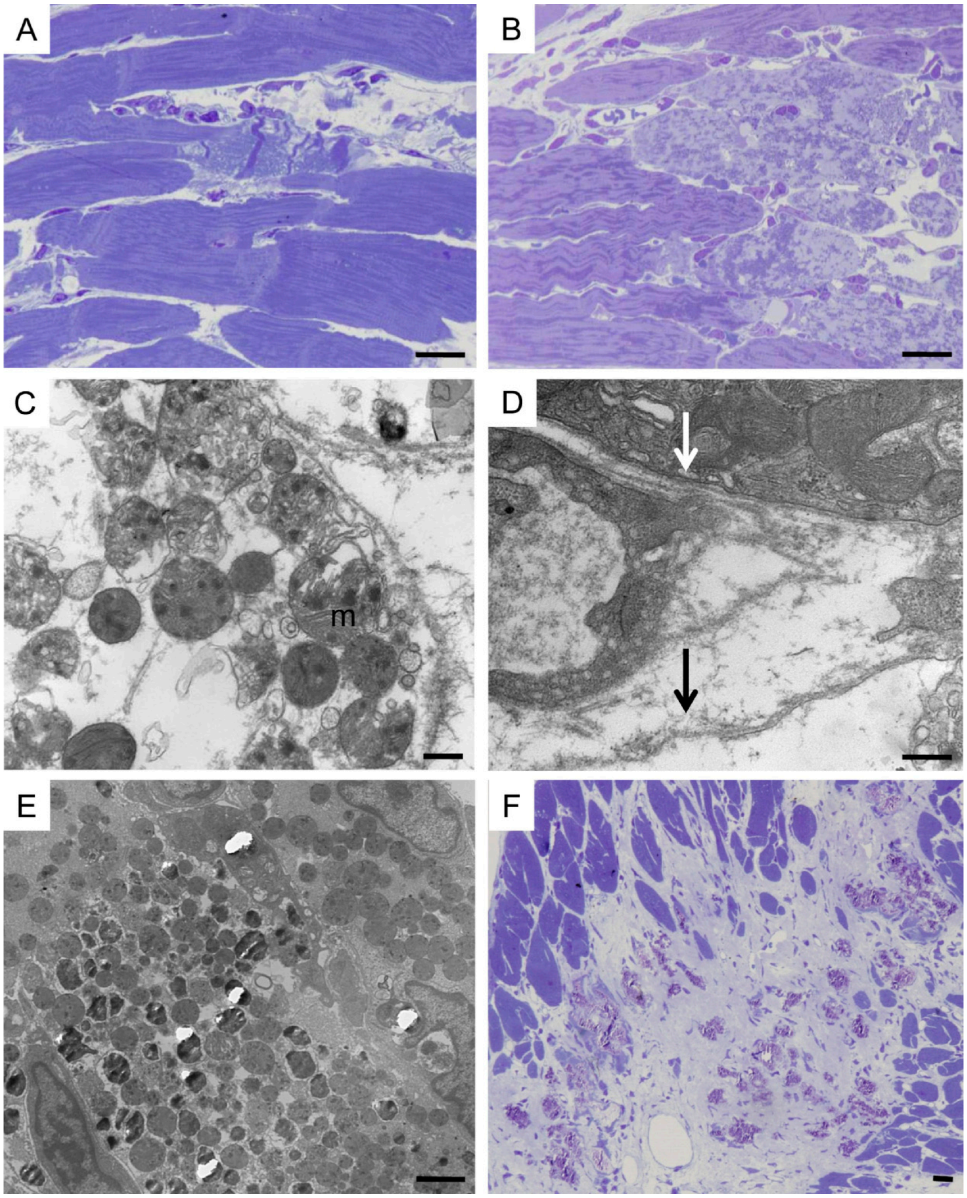

Figure 8. Ultrastructural features of cardiomyocyte necrosis in Tg-NS/H mice. (A) Focal contraction band necrosis on a semithin section. Bar, 10 µm. (B) Myocytolysis on a semithin section. Bar, 10 µm. (C) Disgregation of cytoplasm with loss of myofilaments and woolly bodies inside swollen mitochondria (m), features in keeping with necrotic cell death. Bar, 500 nm. (D) Loss of sarcolemma integrity in a cardiomyocyte (black arrow) with cytoplasmic disgregation, close to abnormal cardiomyocyte with intact sarcolemma (white arrow). Bar, 500 nm. (E) Mineralization of mitochondria. Bar, 2 µm. (F) Spotty calcification within fibrous tissue on a semithin section. Bar, 10 µm.

(Chitaev and Troyanovsky, 1998; Sotomayor and Schulten, 2008). It has been previously shown that point mutation of amino acid residues directly involved in coordinating Ca^{2+} at successive sites between individual ectodomains results in loss of adhesive (trans) intercellular interaction of dimers and favors lateral interaction of ectodomains stemming from the same cell (cis-interaction; Klingelhöfer et al., 2002). Residue N266 (N271 in mouse) of *DSG2*, located between the second and third cadherin ectodomains, represents one of these critical Ca^{2+} coordinating residues (Fig. S3). We observed, however, structurally normal desmosomes both in the human ARVC patient and in Tg-NS/H mice, similar to those observed in WT and Tg-WT mice, without any evidence of gap widening. This is in line with a dominant-negative effect of mutant *DSG2* on desmosome function rather than structure.

An interesting observation from the engineering of mutant mice for desmosomal proteins is that a single nucleotide change associated with amino acid substitution in a key protein function domain is alone able to reproduce the main clinical and pathological features of ARVC, whereas heterozygous gene knockout does not result in disease phenotype (Ruiz et al., 1996; Grossmann et al., 2004). These data are consistent with a dose-dependent dominant-negative effect of the N271S-*dsg2* mutation on cell integrity and ARVC phenotype in transgenic mice, whereas haploinsufficiency alone may not be sufficient to cause disease.

Myocyte necrosis is a key initiator of myocardial dystrophy

Our experimental model for the first time provides evidence that necrotic myocyte death is the initiating event in the myocardial injury and repair process. Necrosis always preceded other pathological signs of disease, such as inflammation and calcification, and later on, fibrosis, ventricular dilation, and aneurysm formation. Furthermore, myocyte necrosis originated in the subepicardial myocardium, followed

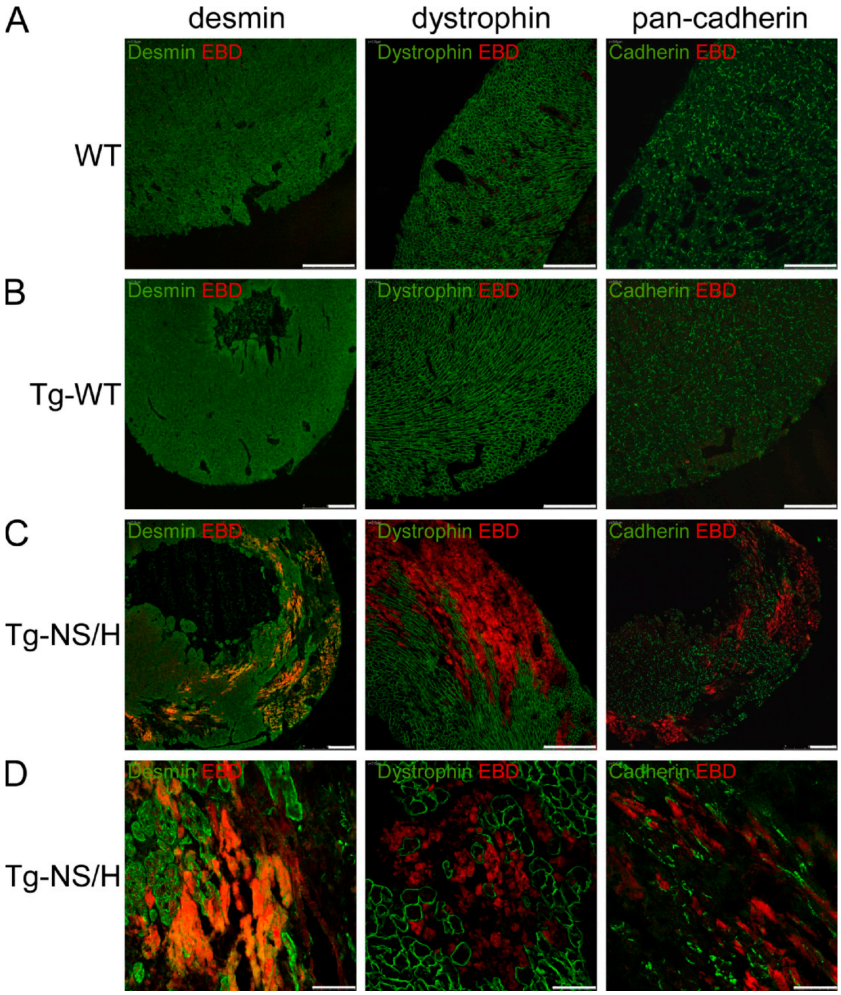

Figure 9. Immunohistochemical analysis of cardiac cryosections from 2–3-wk-old mice injected with EBD. (A and B) WT and Tg-WT hearts show normal distribution of desmin, dystrophin, and pan-cadherin in the ventricles, and no EBD-positive cells. Bars, 250 µm. (C and D) In contrast, hearts from Tg-NS mice display large areas of ventricular myocardium lacking desmin, dystrophin, and pan-cadherin. These abnormal areas contained myocytes positive for EBD, indicating increased cell membrane permeability and loss of myocyte integrity and viability. Bars: (C) 250 µm; (D) 50 µm.

by a wave-front extension toward the endocardium. This wave-front phenomenon of myocardial atrophy is well documented in human ARVC, both by histopathologic examinations and cardiac magnetic resonance studies (Sen-Chowdhry et al., 2008; Basso et al., 2009). The underlying mechanism for this remains unknown, although heterogeneity in transmural distribution of myocardial fiber architecture and/or of wall mechanics may play a role. Apoptosis was also observed in hearts from Tg-NS mice of different ages, but to a smaller extent and usually confined to areas of necrosis or fibrosis, indicating that, although apoptosis can contribute to progressive cardiomyocyte atrophy (Valente et al., 1998),

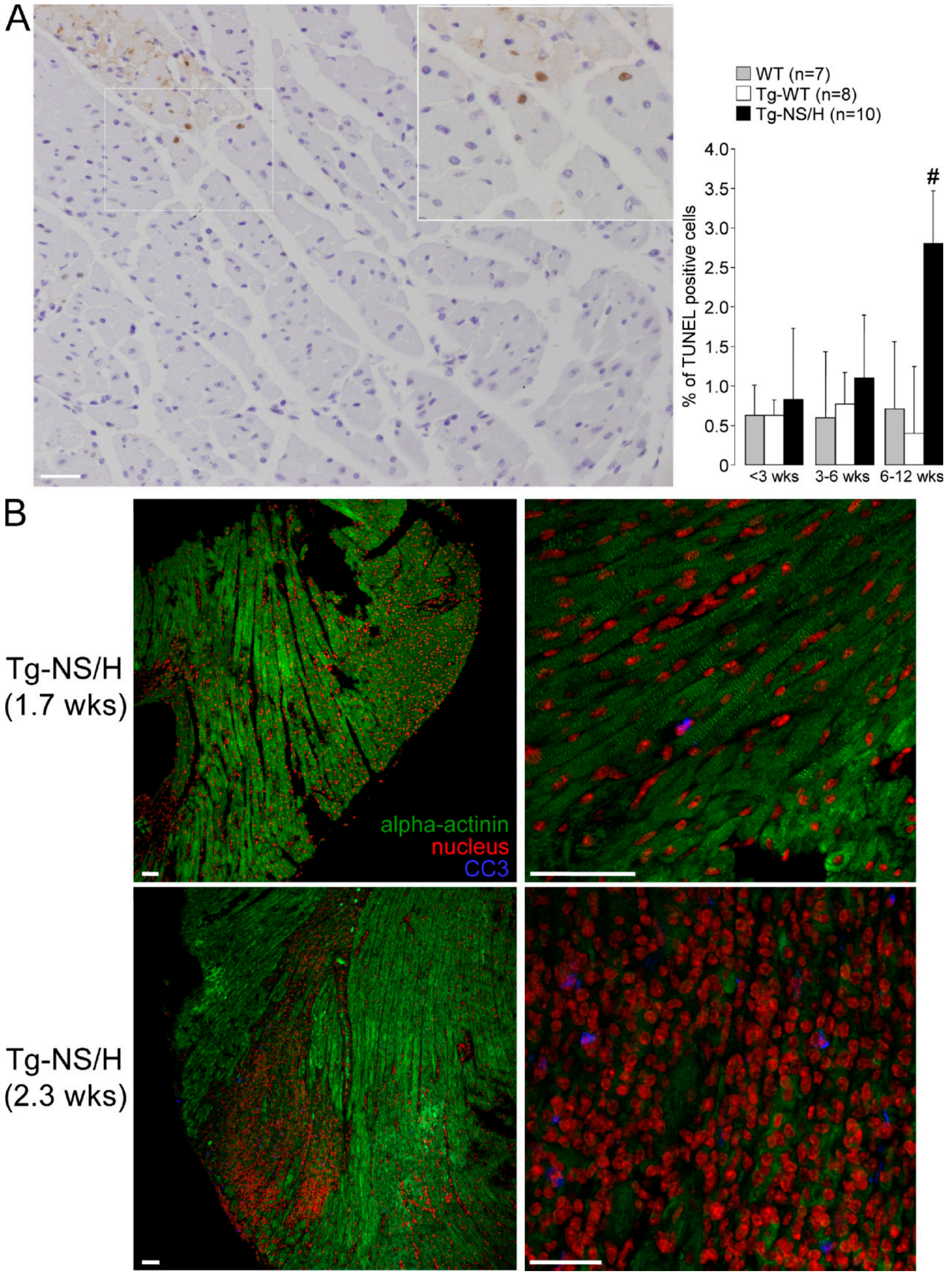

Figure 10. Cardiomyocyte apoptosis in Tg-NS/H mice. (A, left) TUNEL analysis of cardiac apoptosis. Note the presence of positive-stained myocyte nuclei (brown) close to an area of myocyte necrosis. (inset) Close-up of boxed area. Bar, 50 µm. (right) Mean values are depicted for the percentage of TUNEL-positive cells in three age groups. Data in this figure are representative of 7 WT, 8 Tg-WT, and 10 Tg-NS/H mice. #, $P < 0.05$ vs. WT and Tg-WT. (B) Immunohistochemical analysis of cleaved caspase-3 (CC3) for assessment of apoptosis in cardiac cryosections from Tg-NS mice. In Tg-NS mice <2 wk old (1.7 wk old in this example), cardiac structure was still unaltered, as indicated by the normal α-actinin staining pattern, and CC3-positive cells were hardly observed. In contrast, in hearts of Tg-NS mice of >2 wk old, clear CC3 staining was observed, but only in necrotic areas of the ventricular myocardium. Bars, 50 µm.

necrosis appears to be the leading mechanism in disease onset and exacerbation.

Different from previously reported ARVC animal models, in which only the characteristic features of advanced ARVC were reported (Garcia-Gras et al., 2006; Yang et al., 2006), in our *dsg2* model we have performed, for the first time, a "step-by-step" investigation of histopathological changes occurring over time in the myocardium, starting from the stage in which the myocardium appeared normal, through the early stages of myocardial disease, and extending toward the late ARVC phenotype. Overall, this *dsg2* animal model highlights hitherto underexposed aspects of ARVC. However, mutations in the *DSG2* gene account for only a minority of ARVC patients, and the results of the present study may not necessarily be transferable to mutations in other ARVC genes that are much more frequent in the ARVC population (i.e., desmoplakin or plakophilin-2). Further studies are needed to assess whether our findings also hold true for other genetic forms of ARVC.

Necrosis has been rarely observed at postmortem analysis (Basso et al., 1996; Bauce et al., 2005). The fact that necrosis is not often reported in both autopsy and endomyocardial biopsy studies (Basso et al., 2008) of human ARVC likely relates to its focal distribution and possibly episodic nature, typically during disease onset or acute phases of disease progression. In the clinical setting, environmental factors such as exercise or inflammation have been advocated in facilitating disease onset and progression by worsening cell adhesion. In fact, human disease onset and progression is sometimes characterized by the onset of chest pain with electrocardiographic changes and myocardial enzyme release, mimicking acute myocardial infarction so as to suggest underlying cardiomyocyte necrosis (Bauce et al., 2005; Sen-Chowdhry et al., 2008; Basso et al., 2009).

Dystrophic myocardial calcification was detected both in Tg-NS mice and in the explanted human ARVC heart, and has been previously reported both in spontaneous animal models (Protonotarios and Tsatsopoulou, 2004) and in human ARVC (Basso et al., 2001). Although these observations may signify previous episodes of accelerated necrosis, we cannot exclude that dystrophic calcification in the failing heart of the N266S proband resulted from other potential causes beyond those that are integral to the underlying ARVC disease process. In addition, the magnitude of calcification observed in the mouse may reflect an increased susceptibility to calcification caused by active bone mineralization mechanisms in these young rapidly growing animals (Fatkin et al. 1999; Topaz, 1991).

So far, myocyte necrosis and dystrophy have been related to mutation in structural proteins linking the underlying contractile proteins to the sarcolemma and the extracellular matrix or those that stabilize or repair the cell membrane (Bansal et al., 2003; Lapidos et al., 2004). Our findings in Tg-NS mice, together with the presence of pronounced calcification as a sequela of previous necrosis in the explanted heart of the N266S proband, provide the first evidence that myocyte necrosis and dystrophy also stem from intercellular junction proteins. Although the mechanism by which mutant *dsg2* produces myocyte necrosis remains to be elucidated, one could hypothesize that desmosomal protein dysfunction affects sarcolemma integrity and/or mithocondrial permeability with abnormal calcium homeostasis.

Electrical instability, conduction disturbances, and biventricular involvement

Extensive investigation of the electrophysiological consequences of overexpression of *dsg2*-N271S shows a highly arrhythmogenic phenotype, with a high prevalence of spontaneous ventricular arrhythmias. Crucially, arrhythmia inducibility was greatly increased in both the RV and LV, in line with the observed biventricular disease involvement on echocardiography, gross morphology, and histology. The biventricular involvement is not an unexpected finding. The proband with the N266S mutation had left ventricular abnormalities, and genotype–phenotype correlations in ARVC mutation carriers have shown a higher occurrence of LV involvement than previously thought, supporting the adoption of the broader term "arrhythmogenic cardiomyopathy" (Basso et al., 2009).

Sudden death occurred in 30% of mice with high expression of N271S-*dsg2* by the age of 3.6 wk, and only 20% of Tg-NS/H mice survived by the age of 20 wk. Thus, premature death occurs not only in the advanced stages of the disease but also at young age, when there is as yet no morphological evidence of the chronic fibrous repair with aneurysm formation but only of the acute–subacute damage, with myocyte necrosis and inflammation. This again reproduces accurately the clinical course of human ARVC, where cardiac arrest can manifest at every stage along the natural history (Nava et al., 2000). VT/fibrillation is usually the mechanism of instantaneous sudden death in the "hot phase" of disease progression, likely because of acute myocyte death and reactive inflammation (Basso et al., 2009). On the contrary, older patients with a long-lasting ARVC more often experience scar-related VT.

Conduction through the ventricles was clearly affected in Tg-NS mice, whereas sinoatrial and atrioventricular conduction were unaltered. The last finding also reproduces the human disease, in which conduction slowing has been proven to be typically parietal and not septal, because of fibro-fatty replacement of the working myocardium of the ventricular free wall, not affecting the specialized conducting tissue.

Fatty tissue and ARVC mouse models

Clear-cut evidence of adipocytes was never observed neither in routine histology nor in ultrastructural investigation of the myocardium in Tg-NS mice both at early stages of disease onset and in later stages. Only focal neutral lipid accumulation in areas of ongoing myocyte death was evident, suggesting alteration of lipid metabolism. Noteworthy, this was also the case of previous ARVC experimental animal models (Garcia-Gras et al., 2006; Yang et al., 2006), which described only an excess accumulation of fat droplets, predominantly at the site of fibrosis. The absence of adipose tissue in transgenic mice of ARVC might be caused by differences between species, considering that the WT mouse does not show evidence of epicardial fat, which is different from the human heart, where there is always a physiological amount of fatty tissue in the subepicardium.

In conclusion, transgenic mice overexpressing the *dsg2* mutation N271S recapitulate pathognomonic features of human ARVC. Our data demonstrate for the first time that myocyte necrosis is a key initiator of myocardial dystrophy in *dsg2*-related ARVC and represent a starting point for further studies regarding the molecular mechanism of ARVC pathogenesis.

MATERIALS AND METHODS

Clinical evaluation of the ARVC patient. The study was approved by the University of Padua Medical School–Azienda Ospedaliera ethical committee. Informed consent was obtained from the patient, and clinical evaluation consisted of a detailed personal/family history, physical examination, 12-lead ECG, two-dimensional echocardiography, signal-averaged ECG, and stress-test ECG, performed according to previously reported methods (Nava et al., 2000). The relatives of the proband were diagnosed based on the established European Society of Cardiology/International Society and Federation of Cardiology Task Force major and minor criteria (McKenna et al., 1994).

Generation of Tg-NS and Tg-WT mice. *Dsg2* cDNA was amplified by RT-PCR from RNA isolated from cardiac tissue of FVB/N mice (Charles River Laboratories) using forward (5′-TCCCGCAGAGTCAGAGAAG-3′) and reverse (5′-CTTATCGTCATCGTCCTTGATGTCACCTCCA-CCTCCGGAGTAAGAATGTTGCATGGTG-3′) primers designed to generate a FLAG epitope fused to the C terminus of *DSG2* to enable localization of the transgene protein product and differentiation from the endogeneous *dsg2*. The nucleotide change leading to the N271S amino acid substitution was introduced by site-directed mutagenesis using the Quikchange kit (Agilent Technologies) and the following primers: 5′-CCGTATATTGGATGTCAGTGACAATATACCTGTGG-3′ and 5′-CCACAGGTATATTGTCACTGACATCCAATATACGG-3′. WT and N271S mutant *dsg2* cDNA (3.4 kb) were cloned into the α-myosin heavy chain promoter construct (supplied by J. Robbins, Children's Hospital, Cincinnati, OH) for cardiac-specific overexpression. WT and mutant (N271S and NS) sequences were separated from the plasmid backbones by restriction endonuclease digestion and injected into fertilized oocytes of FVB/N mice to generate transgenic mice (Tg-WT and Tg-NS) according to standard procedures. Founder mice were identified by PCR using primers specific for the transgene. Level of transgene expression in the different lines was compared by Western blot analysis on cardiac tissue using anti-FLAG antibody. Founder mice were bred with FVB/N mice and maintained in a pathogen-free environment. Experimental protocols were in accordance with governmental and institutional guidelines for animal use in research and were approved by the Animal Experimentation Commission of the Academic Medical Center (University of Amsterdam).

Echocardiographic analysis. In the patient, the two-dimensional–parasternal short-axis view was obtained at the level of papillary muscles. Wall thickness and dimensions were measured from M-mode images using the leading-edge method on three consecutive cardiac cycles (Rottman et al., 2007). RV measurements derived from the clinical study protocol in humans (Yoerger et al., 2005) were used to quantify RV size and function.

In vivo cardiac morphology and function was assessed in mice under anesthesia (1.5% oxygenated isoflurane inhalation, 37°C body temperature) using a mouse transthoracic echocardiography system equipped with a 30-mHz linear transducer (Vevo770; VisualSonics). Equally aged Tg-NS/H and Tg-NS/L mice were compared with age-matched control WT and Tg-WT mice. Echocardiographic data and images were analyzed off-line by a researcher blinded to the genotype.

ECG measurements. 12-lead ECG in humans was performed according to previously reported methods (Nava et al., 2000). For surface ECG analysis, mice were anaesthetized using isoflurane inhalation (induction 4 volume % in oxygen followed by maintenance 1–1.5 volume %). Four-lead surface ECGs were recorded from subcutaneous 23-gauge needle electrodes attached to each limb using the Powerlab acquisition system (ADInstruments). Leads I and II were analyzed for heart rate (RR interval) and PR, QRS, and QT duration using Chart5 Pro analysis software (ADInstruments). QT intervals in mice were corrected for heart rate using the following formula: QTc = QT/(RR/100)1/2 (RR in ms; Mitchell et al., 1998).

Epicardial mapping experiments. Mice were anesthetized by an intraperitoneal injection of pentobarbital, after which the heart was excised, cannulated, and mounted on a Langendorff perfusion set-up, and epicardial mapping on the RV and LV was performed as previously described (Remme et al., 2006). In short, ventricular extracellular epicardial electrograms were recorded during sinus rhythm and ventricular pacing at 120 ms and at twice the stimulus threshold from the center of the electrode. Inducibility of ventricular arrhythmias was assessed using a stimulation protocol with up to three extrastimuli, followed by burst pacing at the shortest possible coupling intervals.

EBD uptake. 1% EBD (wt/vol; 1 mg /0.1ml PBS/10 mg body weight; Sigma-Aldrich) was administered intraperitoneally at the right side of the peritoneal cavity to 2–3-wk-old mice, after which the animals were returned to their cage and allowed food and water ad libitum. After 24 h, the mice were sacrificed and hearts were excised, snap-frozen in liquid nitrogen, and sectioned into 7-µm-thick cryosections. EBD was detected as red autofluorescence under a fluorescent microscope (Han et al., 2007).

Morphological analysis. For pathological studies, hearts from 30 mice per line at different age groups were isolated and fixed in 10% phosphate-buffered formalin (pH 7.35) for gross and histological examination. Macroscopic evaluation included assessment of chamber dilatation and aneurysms, and measurements of heart weight and wall thickness. 7-µm-thick paraffin-embedded sections were serially cut and routinely stained by H&E to examine the myocardium, by Heidenhain trichrome and Sirius red for assessment of fibrosis, and by von Kossa for the detection of calcium.

Histomorphometric analysis to assess myocyte diameters was performed on samples stained with H&E using an image analyzer system and commercially available software (Image-Pro Plus Version 4.0; Media Cybernetics) according to a previously described method (Basso et al., 2008).

Furthermore, freshly isolated, snap-frozen hearts from five mice per age group were mounted in Tissue-Tek Optimal Cutting Temperature compound (Sakura). 7–8-µm-thick myocardium cryosections were stained with Oil red O and counterstained with H&E to assess the presence of neutral lipids.

Ultrastructural investigation. Myocardial samples (LV and RV separately) were fixed in 2.5% glutaraldehyde in 0.1 mmol/liter of phosphate buffer (pH 7.3) and postfixed in buffered 1% osmium tetroxide for 1 h. Samples were dehydrated in a series of ethanol and embedded in epon. Semithin sections were first evaluated under light microscopy before proceeding with the ultrathin sections. Thin sections were stained with uranyl acetate and lead citrate and examined under an electron microscope (H-7000; Hitachi) equipped with a digital camera. Intercalated discs were assessed at final magnifications of 30,000 and 60,000 according to a standardized method (Basso et al., 2006).

Immunohistochemistry. Cardiac cryosections were prepared, treated, and stained for immunohistochemistry according to standard procedures. The following primary antibodies were used against FLAG (1:100; M5; Sigma-Aldrich), *dsg2* (1:100; Progen), desmocollin-2 (1:100; S-14; Santa

Cruz Biotechnology, Inc.), plakoglobin (1:5; PG5.1; Progen), desmoplakin 1 and 2 (Progen), connexin 43 (1:100; Sigma-Aldrich), plakophilin-2 (2a+2b; Biodesign), pancadherin (1:100; Sigma-Aldrich), desmin (DARD; 1:50), α-actinin (1:1,000; Sigma-Aldrich), cleaved caspase-3 (1:1,000; Asp175; Cell Signaling Technology), and dystrophin (1:250; Abcam), and secondary antibodies were conjugated to Alexa Fluor 488 and Alexa Fluor 594 (1:500; Invitrogen).

TUNEL assessment. Cardiac ventricular tissue of 2-, 3-, 6-, and 12-wk-old Tg-NS, Tg-WT, and WT mice was fixed in formalin, embedded in paraffin, sectioned, and stained for DNA fragmentation by a TUNEL protocol according to the manufacturer's specifications (R&D Systems). Myocardial sections were examined under light microscopy at a magnification of 40, and at least 1,000 myocytes were counted per animal. The apoptotic index was calculated as the number of positive myocytes divided by the total myocyte number and multiplying that value by 100 (Valente et al., 1998).

Western blot analysis. Mouse heart tissue was snap frozen in liquid nitrogen, pulverized, and homogenized in ice-cold lysis buffer (containing 5 mM Tris-HCl [pH 7.5], 2 mM EDTA) supplemented with a protease inhibitor cocktail tablet (Complete Mini; Roche). Total membrane and cytosolic fractions were separated by centrifugation, and the total membrane pellet was resuspended in resuspension buffer (containing 75 mM Tris-HCl [pH 7.5], 5 mM EDTA, 12.5 mM $MgCl_2$, and protease inhibitor cocktail). Protein fraction concentrations were determined by using the BCA protein assay kit (Thermo Fisher Scientific). Subsequently, 80 µg of the (solubilized) protein extracts were treated with Laemmli buffer (containing 25% β-mercaptoethanol) and electrophoresed on SDS-polyacrylamide gels. The gels were blotted to a preequilibrated Immobilon-P polyvinylidene fluoride membrane (Millipore) by means of a semidry system. The total membrane fractions and cytosolic fractions were probed with rabbit polyclonal anti-Flag (1:500; M2; Agilent Technologies) and anti–caspase-3 (1:1,000 dilution; 8G10; Cell Signaling Technology), respectively. Hybridization with anti–α-tubulin served as loading control (1:500; Santa Cruz Biotechnology, Inc.). Secondary antibody (IgG–horseradish peroxidase–linked) signal detection was achieved with a Western blotting detection kit (ECL Plus; GE Healthcare). Antibody signals were visualized using a chemiluminescent image analyzer (LAS-3000 Lite; Fujifilm).

Statistics. Data are presented as means ± SD unless otherwise stated. Where appropriate, the significance of differences between multiple experimental groups was assessed using a nonparametric analysis of variance (ANOVA) test with Bonferroni's posttests, and the significance of differences between two experimental groups was assessed by a Student's *t* test (paired or unpaired as appropriate). $P < 0.05$ was accepted as significant.

Online supplemental material. Fig. S1 describes the generation of Tg-NS and Tg-WT mice. Fig. S2 shows ultrastructural features of intercalated discs in Tg-NS mice. Fig. S3 depicts ectodomain modeling in *dsg2*. Supplemental tables providing additional data from ECG (Tables S1 and S2), echocardiography (Table S3), epicardial mapping (Table S4), and gross and histological data (Table S5) are provided. Online supplemental material is available at http://www.jem.org/cgi/content/full/jem.20090641/DC1.

We thank Dr. M. van Roon for generation of transgenic mice.

This study was supported by the Netherlands Heart Foundation (grant 2008B051); the Registry for Cardio-Cerebro-Vascular-Pathology, Veneto Region, Venice; the Ministry of Education, University, and Research; the Ministry of Health, Rome; and the CARIPARO Foundation, Padua, Italy. During this investigation, Dr. K. Pilichou was a visiting researcher from the University of Padua at the Academic Medical Center, University of Amsterdam. Dr. C.R. Bezzina and Dr. M.J.B. van den Hoff are established investigators of the Netherlands Heart Foundation (grants 2005T024 and 1996M002).

The authors have no conflicting financial interests.

Submitted: 19 March 2009
Accepted: 9 July 2009

REFERENCES

Asimaki, A., P. Syrris, T. Wichter, P. Matthias, J.E. Saffitz, and W.J. McKenna. 2007. A novel dominant mutation in plakoglobin causes arrhythmogenic right ventricular cardiomyopathy. *Am. J. Hum. Genet.* 81:964–973.

Bansal, D., K. Miyake, S.S. Vogel, S. Groh, C.C. Chen, R. Williamson, P.L. McNeil, and K.P. Campbell. 2003. Defective membrane repair in dysferlin-deficient muscular dystrophy. *Nature.* 423:168–172.

Basso, C., G. Thiene, D. Corrado, A. Angelini, A. Nava, and M. Valente. 1996. Arrhythmogenic right ventricular cardiomyopathy. Dysplasia, dystrophy, or myocarditis? *Circulation.* 94:983–991.

Basso, C., A. Tsatsopoulou, G. Thiene, A. Anastasakis, M. Valente, and N. Protonotarios. 2001. "Petrified" right ventricle in long-standing naxos arrhythmogenic right ventricular cardiomyopathy. *Circulation.* 104:E132–E133.

Basso, C., E. Czarnowska, M. Della Barbera, B. Bauce, G. Beffagna, E.K. Wlodarska, K. Pilichou, A. Ramondo, A. Lorenzon, O. Wozniek, et al. 2006. Ultrastructural evidence of intercalated disc remodelling in arrhythmogenic right ventricular cardiomyopathy: an electron microscopy investigation on endomyocardial biopsies. *Eur. Heart J.* 27:1847–1854.

Basso, C., F. Ronco, F. Marcus, A. Abudureheman, S. Rizzo, A.C. Frigo, B. Bauce, F. Maddalena, A. Nava, D. Corrado, et al. 2008. Quantitative assessment of endomyocardial biopsy in arrhythmogenic right ventricular cardiomyopathy/dysplasia: an in vitro validation of diagnostic criteria. *Eur. Heart J.* 29:2760–2771.

Basso, C., D. Corrado, F.I. Marcus, A. Nava, and G. Thiene. 2009. Arrhythmogenic right ventricular cardiomyopathy. *Lancet.* 373: 1289–1300.

Bauce, B., C. Basso, A. Rampazzo, G. Beffagna, L. Daliento, G. Frigo, S. Malacrida, L. Settimo, G. Danieli, G. Thiene, and A. Nava. 2005. Clinical profile of four families with arrhythmogenic right ventricular cardiomyopathy caused by dominant desmoplakin mutations. *Eur. Heart J.* 26:1666–1675.

Chitaev, N.A., and S.M. Troyanovsky. 1997. Direct Ca^{2+}-dependent heterophilic interaction between desmosomal cadherins, desmoglein and desmocollin, contributes to cell–cell adhesion. *J. Cell Biol.* 138:193–201.

Chitaev, N.A., and S.M. Troyanovsky. 1998. Adhesive but not lateral E-cadherin complexes require calcium and catenins for their formation. *J. Cell Biol.* 142:837–846.

Corrado, D., C. Basso, A. Pavei, P. Michieli, M. Schiavon, and G. Thiene. 2006. Trends in sudden cardiovascular death in young competitive athletes after implementation of a preparticipation screening program. *JAMA.* 296:1593–1601.

Fatkin, D., M.E. Christe, O. Aristizabal, B.K. McConnell, S. Srinivasan, F.J. Schoen, C.E. Seidman, D.H. Turnbull, and J.G. Seidman. 1999. Neonatal cardiomyopathy in mice homozygous for the Arg403Gln mutation in the alpha cardiac myosin heavy chain gene. *J. Clin. Invest.* 103:147–153.

Garcia-Gras, E., R. Lombardi, M.J. Giocondo, J.T. Willerson, M.D. Schneider, D.S. Khoury, and A.J. Marian. 2006. Suppression of canonical Wnt/beta-catenin signaling by nuclear plakoglobin recapitulates phenotype of arrhythmogenic right ventricular cardiomyopathy. *J. Clin. Invest.* 116:2012–2021.

Gerull, B., A. Heuser, T. Wichter, M. Paul, C.T. Basson, D.A. McDermott, B.B. Lerman, S.M. Markowitz, P.T. Ellinor, C.A. MacRae, et al. 2004. Mutations in the desmosomal protein plakophilin-2 are common in arrhythmogenic right ventricular cardiomyopathy. *Nat. Genet.* 36:1162–1164.

Grossmann, K.S., C. Grund, J. Huelsken, M. Behrend, B. Erdmann, W.W. Franke, and W. Birchmeier. 2004. Requirement of plakophilin 2 for heart morphogenesis and cardiac junction formation. *J. Cell Biol.* 167:149–160.

Han, R., D. Bansal, K. Miyake, V.P. Muniz, R.M. Weiss, P.L. McNeil, and K.P. Campbell. 2007. Dysferlin-mediated membrane repair protects the heart from stress-induced left ventricular injury. *J. Clin. Invest.* 117:1805–1813.

Kirchhof, P., L. Fabritz, M. Zwiener, H. Witt, M. Schäfers, S. Zellerhoff, M. Paul, T. Athai, K.H. Hiller, H.A. Baba, et al. 2006. Age- and training-dependent development of arrhythmogenic right ventricular cardiomyopathy in heterozygous plakoglobin-deficient mice. *Circulation.* 114:1799–1806.

Klingelhöfer, J., O.Y. Laur, R.B. Troyanovsky, and S.M. Troyanovsky. 2002. Dynamic interplay between adhesive and lateral E-cadherin dimers. *Mol. Cell. Biol.* 22:7449–7458.

Lapidos, K.A., R. Kakkar, and E.M. McNally. 2004. The dystrophin glycoprotein complex: signaling strength and integrity for the sarcolemma. *Circ. Res.* 94:1023–1031.

Mallat, Z., A. Tedgui, F. Fontaliran, R. Frank, M. Durigon, and G. Fontaine. 1996. Evidence of apoptosis in arrhythmogenic right ventricular dysplasia. *N. Engl. J. Med.* 335:1190–1196.

Marcus, F.I., G.H. Fontaine, G. Guiraudon, R. Frank, J.L. Laurenceau, C. Malergue, and Y. Grosgogeat. 1982. Right ventricular dysplasia: a report of 24 adult cases. *Circulation.* 65:384–398.

Marcus, F.I., A. Nava, and G. Thiene, editors. 2007. Arrhythmogenic RV Cardiomyopathy/Dysplasia: Recent Advances. Springer Verlag, Milano. 218 pp.

McKenna, W.J., G. Thiene, A. Nava, F. Fontaliran, C. Blomstrom-Lundqvist, G. Fontaine, and F. Camerini. 1994. Diagnosis of arrhythmogenic right ventricular dysplasia/cardiomyopathy. Task Force of the Working Group Myocardial and Pericardial Disease of the European Society of Cardiology and of the Scientific Council on Cardiomyopathies of the International Society and Federation of Cardiology. *Br. Heart J.* 71:215–218.

McKoy, G., N. Protonotarios, A. Crosby, A. Tsatsopoulou, A. Anastasakis, A. Coonar, M. Norman, C. Baboonian, S. Jeffery, and W.J. McKenna. 2000. Identification of a deletion of plakoglobin in arrhythmogenic right ventricular cardiomyopathy with palmoplantar keratoderma and woolly hair (Naxos disease). *Lancet.* 355:2119–2124.

Mitchell, G.F., A. Jeron, and G. Koren. 1998. Measurement of heart rate and Q-T interval in the conscious mouse. *Am. J. Physiol.* 274:H747–H751.

Nagar, B., M. Overduin, M. Ikura, and J.M. Rini. 1996. Structural basis of calcium-induced E-cadherin rigidification and dimerization. *Nature.* 380:360–364.

Nava, A., B. Bauce, C. Basso, M. Muriago, A. Rampazzo, C. Villanova, L. Daliento, G. Buja, D. Corrado, G.A. Danieli, and G. Thiene. 2000. Clinical profile and long-term follow-up of 37 families with arrhythmogenic right ventricular cardiomyopathy. *J. Am. Coll. Cardiol.* 36:2226–2233.

Norgett, E.E., S.J. Hatsell, L. Carvajal-Huerta, J.C. Cabezas, J. Common, P.E. Purkis, N. Whittock, I.M. Leigh, H.P. Stevens, and D.P. Kelsell. 2000. Recessive mutation in desmoplakin disrupts desmoplakin-intermediate filament interactions and causes dilated cardiomyopathy, woolly hair and keratoderma. *Hum. Mol. Genet.* 9:2761–2766.

Pilichou, K., A. Nava, C. Basso, G. Beffagna, B. Bauce, A. Lorenzon, G. Frigo, A. Vettori, M. Valente, J. Towbin, et al. 2006. Mutations in desmoglein-2 gene are associated with arrhythmogenic right ventricular cardiomyopathy. *Circulation.* 113:1171–1179.

Protonotarios, N., and A. Tsatsopoulou. 2004. Naxos disease and Carvajal syndrome: cardiocutaneous disorders that highlight the pathogenesis and broaden the spectrum of arrhythmogenic right ventricular cardiomyopathy. *Cardiovasc. Pathol.* 13:185–194.

Rampazzo, A., A. Nava, S. Malacrida, G. Beffagna, B. Bauce, V. Rossi, R. Zimbello, B. Simionati, C. Basso, G. Thiene, et al. 2002. Mutation in human desmoplakin domain binding to plakoglobin causes a dominant form of arrhythmogenic right ventricular cardiomyopathy. *Am. J. Hum. Genet.* 71:1200–1206.

Remme, C.A., A.O. Verkerk, D. Nuyens, A.C. van Ginneken, S. van Brunschot, C.N. Belterman, R. Wilders, M.A. van Roon, H.L. Tan, A.A. Wilde, et al. 2006. Overlap syndrome of cardiac sodium channel disease in mice carrying the equivalent mutation of human SCN5A-1795insD. *Circulation.* 114:2584–2594.

Rottman, J.N., G. Ni, and M. Brown. 2007. Echocardiographic evaluation of ventricular function in mice. *Echocardiography.* 24:83–89.

Ruiz, P., V. Brinkmann, B. Ledermann, M. Behrend, C. Grund, C. Thalhammer, F. Vogel, C. Birchmeier, U. Günthert, W.W. Franke, and W. Birchmeier. 1996. Targeted mutation of plakoglobin in mice reveals essential functions of desmosomes in the embryonic heart. *J. Cell Biol.* 135:215–225.

Sen-Chowdhry, S., P. Syrris, S.K. Prasad, S.E. Hughes, R. Merrifield, D. Ward, D.J. Pennell, and W.J. McKenna. 2008. Left-dominant arrhythmogenic cardiomyopathy: an under-recognized clinical entity. *J. Am. Coll. Cardiol.* 52:2175–2187.

Sotomayor, M., and K. Schulten. 2008. The allosteric role of the Ca2+ switch in adhesion and elasticity of C-cadherin. *Biophys. J.* 94:4621–4633.

Stokes, D.L. 2007. Desmosomes from a structural perspective. *Curr. Opin. Cell Biol.* 19:565–571.

Syrris, P., D. Ward, A. Evans, A. Asimaki, E. Gandjbakhch, S. Sen-Chowdhry, and W.J. McKenna. 2006. Arrhythmogenic right ventricular dysplasia/cardiomyopathy associated with mutations in the desmosomal gene desmocollin-2. *Am. J. Hum. Genet.* 79:978–984.

Thiene, G., A. Nava, D. Corrado, L. Rossi, and N. Pennelli. 1988. Right ventricular cardiomyopathy and sudden death in young people. *N. Engl. J. Med.* 318:129–133.

Thiene, G., D. Corrado, A. Nava, L. Rossi, A. Poletti, G.M. Boffa, L. Daliento, and N. Pennelli. 1991. Right ventricular cardiomyopathy: is there evidence of an inflammatory aetiology? *Eur. Heart J.* 12(Suppl. D):22–25.

Topaz, O. 1991. Myocardial calcifications in neonates and infants: a unique tissue reaction. *South. Med. J.* 84:891–895.

Troyanovsky, S.M., L.G. Eshkind, R.B. Troyanovsky, R.E. Leube, and W.W. Franke. 1993. Contributions of cytoplasmic domains of desmosomal cadherins to desmosome assembly and intermediate filament anchorage. *Cell.* 72:561–574.

Valente, M., F. Calabrese, G. Thiene, A. Angelini, C. Basso, A. Nava, and L. Rossi. 1998. In vivo evidence of apoptosis in arrhythmogenic right ventricular cardiomyopathy. *Am. J. Pathol.* 152:479–484.

Yang, Z., N.E. Bowles, S.E. Scherer, M.D. Taylor, D.L. Kearney, S. Ge, V.V. Nadvoretskiy, G. DeFreitas, B. Carabello, L.I. Brandon, et al. 2006. Desmosomal dysfunction due to mutations in desmoplakin causes arrhythmogenic right ventricular dysplasia/cardiomyopathy. *Circ. Res.* 99:646–655.

Yoerger, D.M., F. Marcus, D. Sherrill, H. Calkins, J.A. Towbin, W. Zareba, and M.H. Picard; Multidisciplinary Study of Right Ventricular Dysplasia Investigators. 2005. Echocardiographic findings in patients meeting task force criteria for arrhythmogenic right ventricular dysplasia: new insights from the multidisciplinary study of right ventricular dysplasia. *J. Am. Coll. Cardiol.* 45:860–865.